Advances in Edge Sensors for the Thirty Meter Telescope Primary Mirror

Chris Shelton[a], Terry Mast[b], Gary Chanan[c], Jerry Nelson[b], Lewis C Roberts, Jr.[a],
Mitchell Troy[a], Mark J. Sirota[d], Byoung-Joon Seo[a], Daniel R. MacDonald[a]
[a]Jet Propulsion Laboratory, California Institute of Technology, Pasadena CA 91109, USA;
[b]University of California, Santa Cruz, Santa Cruz CA 95064, USA;
[c]Department of Physics and Astronomy, University of California Irvine, Irvine CA 92697, USA;
[d]Thirty Meter Telescope Corporation, Pasadena CA 91107, USA

ABSTRACT

The out-of-plane degrees of freedom (piston, tip, and tilt) of each of the 492 segments in the Thirty Meter Telescope primary mirror will be actively controlled using three actuators per segment and two edge sensors along each inter-segment gap. We address two important topics for this system: edge sensor design, and the correction of fabrication and installation errors.

The primary mirror segments are passively constrained in the three lateral degrees of freedom. We evaluate the segment lateral motions due to the changing gravity vector and temperature, using site temperature and wind data, thermal modeling, and finite-element analysis.

Sensor fabrication and installation errors combined with these lateral motions will induce errors in the sensor readings. We evaluate these errors for a capacitive sensor design as a function of dihedral angle sensitivity. We also describe operational scenarios for using the Alignment and Phasing System to correct the sensor readings for errors associated with fabrication and installation.

Keywords: Extremely Large Telescopes, edge sensors, segmented mirrors, capacitive sensor

1. INTRODUCTION

The 492 hexagonal mirror segments that form the 30-meter Thirty Meter Telescope (TMT) primary mirror (M1) must be precisely positioned with respect to each other to form a useful optical image. The M1 control system (M1CS) performs this task, with actuators that move segments in tip, tilt and piston relative to the mirror support structure.[1,2,3,4] These movements are based on error signals generated from edge sensors that are exquisitely sensitive to the relative height and tilt of neighboring segments.[5,6,7]

While the segments are actively controlled in optical surface height, lateral motion is only passively constrained, by the backing structure. Thus there will be some small change in the gaps between segments, and some "shear" (segment-to-segment relative motion along an edge), as changing telescope orientation and temperature make small distortions in the steel backing structure. These "in-plane" motions place an additional performance burden on the segment edge sensors, and on the precision with which they must be mounted relative to the optical surface. Errors in the installation of the edge sensors causes in-plane motions to be cross coupled into false height readings.

Some of these reading errors are purely geometric, and independent of sensor type, and some are sensor-dependent. All must be taken into account to stay within the TMT sensor edge height error budget of 5 nm.[8] Limiting the false height readings to less than the 5 nm of surface error purely by eliminating installation errors is unrealistic due to the very small tolerances that result. A method of calibrating the sensors' installation errors is required, one that minimizes the time taken away from collecting science data. Thus there is strong motivation for having an effective and efficient M1CS calibration procedure.

Our approach for correcting gravity- and temperature-induced errors in the M1 control system has three parts. First, the edge sensors are modified to report segment-to-segment gap, as well as the height difference, to give observability to the in-plane segment positions. Second, the telescope is aligned, or "phased", using the Alignment and Phasing System

(APS) on bright stars,[9,10] at a sufficient set of zenith angles and temperatures. Third, a "calibration procedure" is applied.

In this paper, we will present this calibration procedure and estimate its performance with practical levels of sensor mounting tolerances. We will explore what will constitute a sufficient set of zenith angles and temperatures for adequate calibration.

2. M1CS EDGE SENSORS

The TMT edge sensors have a drive half, or transmitter, mounted on one segment edge, and a mating sense half , or receiver, mounted on a neighboring segment edge. The two sensor halves have a coordinate system relative to each other, which is fixed, in our current convention, to the center of the sense half. In this coordinate system, "sensor y" points from the center of the sense half towards the drive half, "sensor z" is towards the sky, normal to the mirror surface and "sensor x" points parallel to the segment edge, forming a right-handed coordinate system. Rotations are defined in the usual way. For example, θ_x, is a rotation around the sensor x axis. It is equivalent to "tilt" or "dihedral angle". Figure 1 illustrates sensor coordinates and shows the locations of the sensors on the mirror segments.

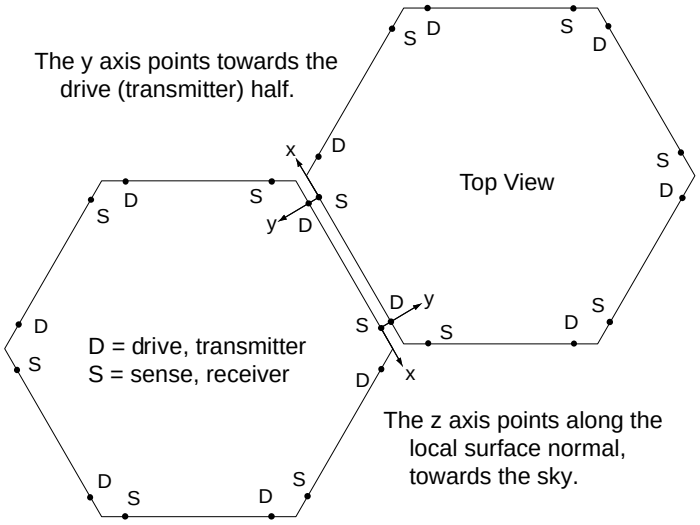

Figure 1 Sensor Coordinate Definitions

2.1 Overview and Common Requirements

While this study focuses on capacitive sensors, this section gives a brief overview of the considerations in common to the capacitive, inductive and optical sensors that are under review for TMT. The candidate edge sensors for TMT all share a geometry in which there are two sensors per edge on neighboring mirror segments.

2.1.1 Non-Interlocking Design

A major design driver is the wish to have a non-interlocking sensor pair (transmit and receive), so that the removal of segments will not require the manipulation of any moving or removable parts. At the Keck telescopes, the edge sensors have an arm, or "paddle", which swings out of the way when a segment is exchanged (Figure 2, right). While this is workable with an array of 36 mirrors, it was felt that it would be too labor intensive with an array of 492 segments. Thus a requirement is imposed to have a non-interlocking design, and, by implication, no moving or movable parts.

2.1.2 Dihedral Angle Sensitivity

Focus mode is the first non-singular mode of the control model of M1[2,6]. It can be envisioned as a change in the radius of curvature of the surface defined by all the segment centers. Neighboring segment edges remain lined up in height, so sensors which only see height find this mode unobservable.

To first order, an error in focus mode is an error in telescope focus. In the geometric approximation, images from the individual segments "unstack", and move away from each other. Refocusing the telescope, by moving the secondary, putting focus on a deformable mirror, etc., can correct for much of the wavefront error due to focus mode.

The residual wavefront error after focus mode has been corrected by telescope refocusing, called scalloping, is caused by the mismatch between the segment's local radius of curvature and the adjusted mirror figure. It is called scalloping because a plot of the residual error across M1 shows a series of small, shallow parabolas, one for each segment.

To make focus mode observable on the Keck telescope, the edge sensors are arranged to measure height not at the mirror segment edge, but 55 mm from the edge, offset by the effective length of the paddle arm. Alternate sensors are offset in opposite directions. The effect of this geometry is to create a sensor whose output, or "reading", is proportional to both height (z) and dihedral angle (θ_x).

$$R \propto z + L_{eff}\theta_x \tag{1}$$

The ratio of height to dihedral angle sensitivity is called L_{eff}, the "effective lever arm". It has the units of nm/μrad, or equivalently, mm. In the Keck design, L_{eff} is a physical 55mm distance.

The focus mode situation for TMT is more complex than for Keck. Eliminating the physical lever arm creates a challenge to obtain dihedral angle sensitivity by alternate means. The increase in number of segments from 36 to 492 creates dynamic range and precision issues in the control laws, on the one hand, but considerably reduces the scalloping residual, on the other. All science observations will have either active-optic or adaptive-optic wavefront sensors, which provide focus tracking. For these and other reasons, TMT focus mode control and error budget are the subject of ongoing study.[11,12] For the purposes of the current paper, we will use a provisional target value of dihedral angle sensitivity of 15 nm/μrad, or L_{eff} = 15 mm.

2.1.3 Low Sensitivity to Humidity and Dust

Experience at Keck plus laboratory experiments[13] have shown that environmental protection is needed for capacitive sensors, in the form an elastic boot or seal. Optical sensors will need a light seal, and may need an environmental boot as well. One attraction of inductive sensors is the possible elimination of such a boot, and its need for removal during segment exchanges.

2.1.4 Gap Invariance and Gap Measurement

As discussed in Sec. 4, the gap between segments can vary by up to 270 μm dynamically, with another half millimeter or so of segment installation tolerance. All sensors need some way to correct or compensate gap dependence, or to be intrinsically insensitive to gap changes. At least for capacitive and inductive sensors, this means a built-in gap measurement capability.

2.1.5 Long-term Stability and Adequate Noise Performance

The baseline operational plan for TMT is that some segments will be exchanged for recoating every two weeks, with some expectation that improvements in coating technology will allow recoating every four weeks. The M1CS is expected to provide good mirror figure for either duration. The current error budget allows 5 nm of noise and 1 nm/week of drift.[8]

3. CAPACITIVE EDGE SENSORS

A capacitive sensor has one or more drive plates excited with AC voltages, which induce AC currents in one or more sense plates. In both the Keck and the TMT geometries, there are two drive plates, driven with equal and opposite square waves of about 6V amplitude. Likewise there is one sense plate that sees an induced current with a sign and magnitude proportional to any displacement from the plane of symmetry.

The TMT capacitive sensor prototype[5,6,7], shown on the left side of Figure 2 and in Figure 3, has a face-on design allowing segment exchange without moving sensor parts.

The right side of Figure 2 shows a Keck sensor, with its arm, the central electrode, that swings out of the way when a segment is exchanged. The effective sensor location is under one of the segments, offset by 55 mm from the gap

between segments. This introduces a desired sensitivity to dihedral angle, with L_{eff} = 55mm. In the Keck geometry, L_{eff} is not a function of gap.

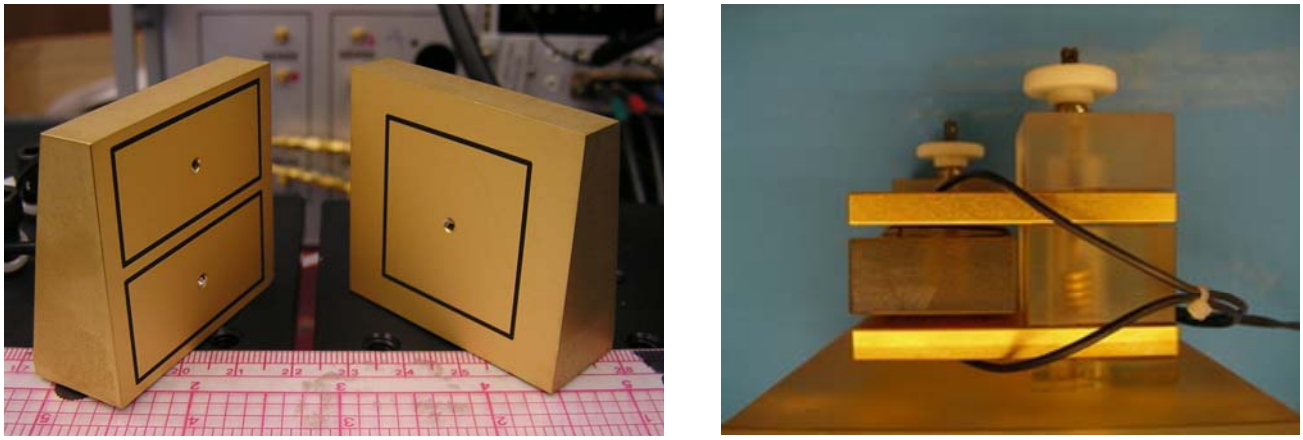

Figure 2. TMT Prototype Capacitive Sensor (left) and Keck Capacitive Sensor (right)

3.1 Capacitive Sensor Sensitivities

In the TMT capacitive sensor geometry, height sensitivity arises from varying the effective plate area, and tilt sensitivity arises from varying the effective plate spacing.

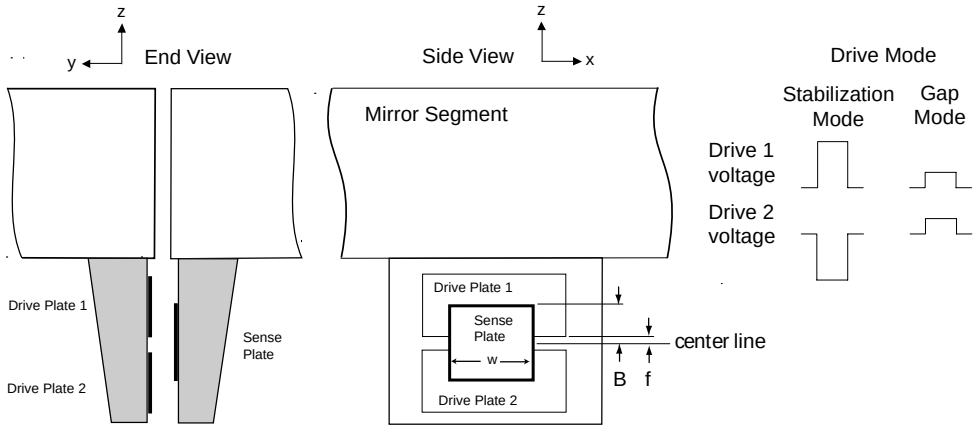

Figure 3. TMT capacitive edge sensor.

Using a simple parallel-plate analysis, an equation can be written for the sensor reading vs height, tilt and installation errors.

$$R = \frac{2\varepsilon_0 wV}{y}\left(-z - z^D + z^S - x\left(\theta_y + \theta_y^D\right) - y\theta_x^S + \frac{B^2 - f^2}{2y}\left(\theta_x + \theta_x^D - \theta_x^S\right)\right) \qquad (2)$$

The desired sensitivities are to height, z, and to dihedral angle, θ_x. The undesired sensitivities are to displacements x and y, and to installation error angles $\theta_x^D, \theta_x^S, \theta_y^D, \theta_y^S$, with separate bookkeeping for the drive (D) and sense (S) side.

The other variables are:

R	Sensor reading per drive edge (coulombs)
ε_0	8.854 10^{-12} farads / meter
w	Sense plate width (30 mm)
V	Drive amplitude (6V)
2B	Sense plate height (30 or 20.8 mm, depending on desired L_{eff})
2f	Gap between drive plates (4 mm)
y	Gap from drive to sense (3.5 +/- 1.2 mm).

The dihedral angle sensitivity is given by

$$L_{eff} = \frac{B^2 - f^2}{2y} \tag{3}$$

Notice that L_{eff} is a strong function of the sensor gap. This is a significant complication.

The prototype sensor was built with sense plate height of 30 mm. With the current nominal sensor gap of 3.5 mm this gives an L_{eff} of 31.6 mm. In this analysis we will consider both an L_{eff} of 31.6 mm, and also an L_{eff} of 15 mm, corresponding to a sense plate height of 20.8 mm.

The sensor calibration scheme as currently formulated assumes small sensor motions around a baseline position, modeled as in Eq. 4.

$$\delta R = c_x \delta x + c_y \delta y \tag{4}$$

The model requires partial derivatives of sensor reading, Eq. 2, with respect to x and y, evaluated at $x, y, z, \theta_x, \theta_y, \theta_z = 0$. Equations 5 and 6 are these derivatives.

$$c_x = -\frac{2\varepsilon_0 wV}{y}\theta_y^D \tag{5}$$

$$c_y = -\frac{2\varepsilon_0 wV}{y^3}\left(B^2 - f^2\right)\left(\theta_x^D - \theta_x^S\right) \tag{6}$$

4. CALCULATION OF SENSOR IN-PLANE MOTIONS

4.1 In-plane motions due to gravity

An existing finite-element-analysis (FEA) of the telescope[14] was used to estimate the in-plane motions due to gravity at sensor locations. This analysis produced tabulated segment displacements and rotations, relative to no gravity, for zenith angles of 0°, 30°, and 65°. A zenith angle of 30° was treated as a baseline and subtracted from the 0° and 65° data. We then transformed the data from the segment-center coordinates to sensor coordinates, with results as shown in Table 1. The maximum sensor-y (gap) change is 0.27 mm, and the maximum sensor-x (parallel to edge) change is 0.19 mm.

Table 1. Summary of Segment In-plane Motions Due to Gravity. These are RMS and maximum absolute segment-to-segment motions, evaluated at sensor locations, for 2772 sensors, in sensor coordinates. Sensor-x is along the segment edge and sensor-y is the gap dimension. Motions are relative to segment positions at 30 degrees zenith.

	RMS	MaxAbs	
Sensor-x, 0 degrees	0.035	0.16	mm
Sensor-x, 65 degrees	0.042	0.19	mm
Sensor-y, 0 degrees	0.040	0.23	mm
Sensor-y, 65 degrees	0.052	0.27	mm

The distribution of motions has a fairly narrow central core, with outliers at higher displacements corresponding to the regions of the mirror with higher stress, typically near the attachment of the elevation bearing.

Finally, we fit the sensor positions to an analytical model as a function of zenith angle, as in

$$\delta x_n(z) = c_{1n}^x \cos(z) + c_{2n}^x \sin(z) \tag{7}$$

$$\delta y_n(z) = c_{1n}^y \cos(z) + c_{2n}^y \sin(z), \tag{8}$$

where δx and δy are the changes in sensor x and y coordinate, z is the zenith angle, and c_x and c_y are coefficients that depend on the sensor number. By convention, the positions are relative to positions at a selected zenith angle, in this case 30 degrees.

4.2 In-plane motions due to temperature

Changes in temperature will move the mirror segments by causing expansion or contraction in the steel backing structure of the segments. To analyze the amount of motion, we used the modeled temperature environment of the TMT mirror. These were based upon one year of free-air temperatures collected at the baseline TMT site of Armazones.[15] For the year of Armazones data used, the observed maximum temperature excursion in any two week period is 9.0°C, and the range over the whole year is 14°C.

While more detailed thermal model can be incorporated as future work, for now we model the effect of temperature on the M1 support structure as global expansion and contraction. Assuming thermal expansion is uniform across the primary mirror as the steel backing structure expands or contracts, there is no change in shear, but only a change in the gap. The change in gap is, $\Delta y = k\Delta T$, where the expansion constant k is 16.8 μm/°C. It is the product of the expansion coefficient of the steel structure, 11.7 ppm/°C and the center-to-center segment spacing of 1.44 m. The 9°C maximum temperature excursion then gives a maximum gap deviation (sensor-y) of 152 μm.

4.3 Combined Analytical Model

For the purpose of estimating the performance of a sensor calibration scheme, we simply sum the zenith angle and temperature models. The temperature model relates thermal expansion to a baseline temperature T_0.

$$\delta x_n(z,T) = c_{1n}^x \cos(z) + c_{2n}^x \sin(z) \tag{9}$$

$$\delta y_n(z,T) = c_{1n}^y \cos(z) + c_{2n}^y \sin(z) + k(T - T_0), \tag{10}$$

The justification for this simple linearized model is that sensor motions are always evaluated with respect to some APS run where the mirror is known to be phased correctly, so the motions are small, and the temperature is T_0. The proper selection of which APS run to call the baseline also helps to keep these changes small.

4.4 In-plane Positions from Gap Measurement

The TMT edge sensors are designed not only to measure the relative piston between segments, but also to measure the segment-to-segment gap (sensor y). This is to enable calculation of the in-plane segment motions, and from them derive the sensor shear motions (sensor x). The method[16] can be understood by imagining "virtual actuators", which can generate the three segment in-plane motions (segment x), (segment y) and (segment rotation). We exercise these virtual actuators to find the single-segment 12 x 3 g-matrix that relates in-plane motions to sensor gap changes (sensor y). We do the same to find the single-segment 12 x 3 h-matrix that relates virtual actuators to sensor shear changes (sensor x).

Let us express the 3 in-plane degrees of freedom of the 492 segments as a single (1x1476) vector called s. Let us also expand the g and h local matrices to global (2772 x 1476) G and H matrices, where 2772 is the number of sensors. We can then write

$$\begin{aligned} y &= Gs \\ x &= Hs \end{aligned} \tag{11}$$

where y is the (1x2772) vector of the sensor gaps, and x is the (1x2772) vector of the sensor shears.

Finally the G-matrix is inverted, via singular value decomposition, to form a pseudo-inverse G^{-1}. This can be used to calculate 1476 segment motions which are a best fit in the least-squares sense to the 2772 measured gap readings. Call the best-fit segment motions s_{fit},

$$s_{fit} = G^{-1} y_{measured} \tag{12}$$

We can then compute the shear displacements (sensor x) from the gap displacements (sensor y) using

$$\begin{aligned} x_{calculated} &= H s_{fit} \\ x_{calculated} &= H G^{-1} y_{measured} \end{aligned} \tag{13}$$

In one approach, the measured y and calculated x vectors are then used in the rest of the calibration procedure. In the another approach, there is one more step of creating a calculated y vector,

$$\begin{aligned} y_{calculated} &= G s_{fit} \\ y_{calculated} &= G G^{-1} y_{measured} \end{aligned} \tag{14}$$

In this approach, the calculated y vector, instead of the measured y vector, is then used in the rest of the calibration procedure. This projects out sensor reading combinations which do not correspond to physical segment motions (null modes), and thus may provide some noise benefit, which is not estimated here.

The difference between $y_{calculated}$ and $y_{measured}$ may also be helpful in identifying failed or failing sensors. A similar null-vector projection may be performed on the sensor height readings, for similar reasons.

5. CALIBRATION METHODS

5.1 The Alignment and Phasing System: Coarse and Fine Alignment

The Alignment and Phasing System[8,9] (APS) is responsible for surface shape measurement and adjustment of primary mirror (M1), secondary mirror (M2) and tertiary mirror (M3). APS is a Shack-Hartmann sensor, mounted on one of the two Nasmyth Platforms. It will use starlight to measure the wavefront errors and then will send commands to the mirror actuators to align the optics.

The active optics system relies on APS to establish desired sensor readings for each sensor at different zenith angles and temperatures. The APS makes wavefront and interferometric measurements to estimate the shape and position of the optical surfaces. Based on these measurements, the Telescope Control System establishes a flexure model in the form of look up tables for all active optics actuators, not just on M1 but also M2 and M3. The flexure model can be perceived as an "off-line" optical feedback loop with extremely low update rate, expected to be every four weeks, or when segments are exchanged, whichever is sooner. On M1, the APS will measure segment tip/tilts, edge steps between adjacent segments, and the shape of the segments.

To limit drifts in the active optics system and correct small errors not completely accounted for by the pointing and flexure models, seeing-limited science instruments will have on-board wavefront sensors which will provide time averaged on-axis wavefront errors to the active optics system.

APS has several modes with a variety of capture ranges of segment piston and segment tip/tilt. The coarsest mode of APS will have a capture range of 10 arcseconds of tip/tilt on the sky and 200 μm of piston, while the finest mode will have a capture range of 1 arcseconds of tip/tilt and 200 nm of piston. It is expected that a data collection in fine mode will take 0.5 hour, while alignment after a segment exchange (coarse mode) will take up to 2 hours. After APS alignment, the relative segment piston error is 5 nm RMS surface. This APS piston error is an important parameter in the calibration procedure, and should be distinguished from the edge sensor noise, which is, coincidentally, 5 nm.

5.2 Using APS Data to Evaluate Sensor Correction Coefficients

The first step of the calibration process is to carry out several APS runs at a variety of both elevation angles and temperatures. For each APS run, the sensor set points are set equal to the sensor height readings after the segment height

differences are optically nulled out. In addition to the sensor set points, the sensor gap readings are recorded. The in-plane positions of the sensors are then computed using Eqs. 13 and 14.

Once all the APS runs are complete, the sensor set points and the sensor in-plane positions are used to compute the sensor correction coefficients. Sensor correction coefficients, when multiplied by sensor in-plane motions, give a correction to the sensor reading. This correction is continuously computed and applied for each sensor as the telescope tracks an object, taking into account both changes in zenith angle and temperature.

Our goals were to show that we could produce a technique to calibrate the edge sensors as the telescope tracked an object, and also to define installation tolerances for the sensors. To do this, we set up a simulation of the calibration process. First we designated several zenith angles and temperatures at which we would simulate APS runs. The gap and shear motions of each sensor were then computed for those angles and temperatures. The gap and shear as a function of zenith angle were then fit, accurately, by the analytical model of Eqs. 7 and 8. As discussed in Section 4.2, the effects of temperature were added as a simple expansion of the steel backing structure. In this approximation, only gap, and not shear, is a function of temperature. There is also a known clocking of the segments as the temperature changes.[14] This effect was considered secondary and will be added to the simulation at a latter date. One APS elevation angle and temperature combination is considered the baseline and the motions are computed relative to that.

The simulated sensor readings are modeled using Eq 4, and the simulated in-plane motions. The c_x and c_y, coefficients are from Eqs. 5, 6. The sensor installation errors were modeled as independent Gaussian distributions of specified width. We also added Gaussian noise to both the APS readings and the gap readings.

For each sensor, we then have a set of readings and a set of in-plane positions for each the different APS runs. We then use these to solve for the sensor correction coefficients c_x and c_y. This constitutes the sensor "calibration." As a check, we confirmed that we perfectly reconstruct the c_x and c_y when the noise terms were set to zero

With these sensor correction coefficients, we can then correct the edge sensors desired sensor readings when the telescope is at an arbitrary zenith angle and temperature during an observation. Eq. 4 is used again, but the δx and δy are computed by using the modeled sensor positions at the zenith angle and temperature of the observations. The calibration correction is computed using every APS run in turn as a baseline, and the APS run with the smallest sensor correction is chosen. This defines the APS run "nearest" in some sense to the observing condition, in the 2D space of zenith angle and temperature. This smallest correction is then applied to the desired sensor readings of the chosen baseline APS run, to give "corrected desired sensor readings".

6. PERFORMANCE OF THE CALIBRATION PROCEDURE

We define "calibration error" as the difference between Eq. 4 evaluated with the actual, or true, c_x and c_y, and the same equation evaluated with c_x and c_y derived from the APS runs plus the calibration procedure. In this context, "actual, or true", of course means the c_x and c_y of a modeled sensor with a particular instance of installation errors.

In Sec. 6.1, we evaluate this calibration error as a function of the number and parameters of the APS runs and in Sec. 6.2 we explore the effect of changing the magnitude of sensor installation errors. In both sections, the sensor noise in the measurement of gap is modeled as 1 μm rms.

6.1 Performance by APS Scenario

In this section, which evaluates the calibration error as a function of the number and parameters of the APS runs, sensor installation errors and L_{eff} have been kept invariant in magnitude, while observing temperature and zenith angle are varied. Installation errors are modeled with a gaussian distribution of 100 μrad rms in both θ_x (also called "tilt", additive to dihedral angle) and in θ_y (also called "twist"), with uncorrelated errors on drive and sense halves. L_{eff} is kept constant at 15 mm.

The calibration error was evaluated for zenith angles from 0° to 65°, and temperatures over a span of 10°C, for a variety of APS scenarios, and a selection of sensor installation errors. The resulting large data structures were reduced for display purposes by computing either the RMS absolute error, or maximum absolute error, across the 2772 sensors, for each angle and temperature. These are presented as contour plots of the calibration error in nm as a function of zenith angle and temperature.

Figure 4 shows the effect of a single APS run with no calibration applied. The figure shows the edge sensor error as a function of both zenith angle and temperature of science observations. The white circle marks the location of the APS run. The left hand figure shows the RMS error from all 2772 sensors, while the right hand figure shows the error for the sensor with the largest total absolute error. This figure style is used throughout this section.

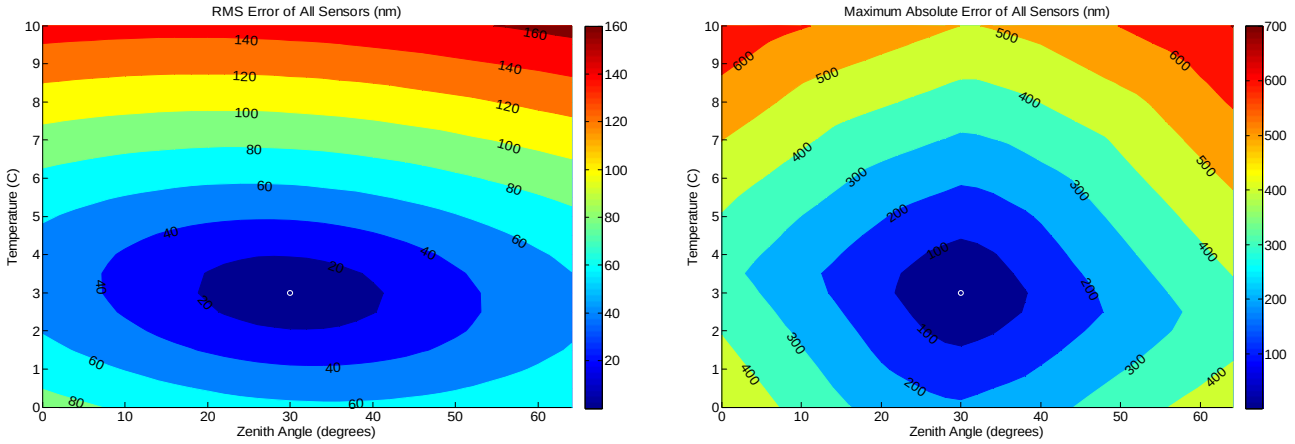

Figure 4. RMS (left) and Maximum (right) Absolute Edge Sensor Error (nm), with 100 µrad rms sensor installation error and 5nm rms APS noise. No calibration procedure is applied. APS zenith angle and temperature is 30 degrees and 3° C. The white circle marks the location of the APS run.

With no calibration, and observing after a single APS run, the calibration error far exceeds the required 5 nm. The error increases as the zenith angle and the temperature of the observations deviate from that of the APS run.

Figure 5 is the result of invoking the calibration procedure. It uses two APS runs taken at different zenith angles, but at the same temperature. Subsequent observations at similar temperatures have decent performance, but the error increases dramatically as the temperature deviates from that of the APS run. The data from Section 4.2 shows that we can expect to experience a peak temperature excursion of 9°C between APS runs. Clearly taking APS runs at only one temperature will provide incomplete calibration.

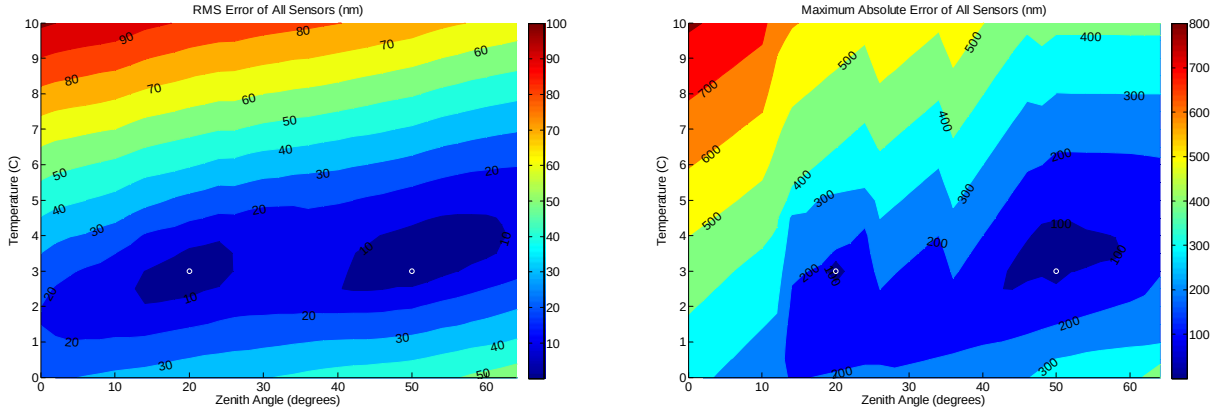

Figure 5. RMS (left) and Maximum (right) Absolute Calibration Error (nm), with 100 µrad rms sensor installation error and 5nm rms APS noise. APS zenith angles and temperatures are 20°, 50° and 3°, 3° C. The white circles mark the location of the APS runs.

Figure 6 shows that adding additional APS runs with both temperature and zenith angle diversity improves the calibration process. In this case there are four runs with zenith angles of 20°, 50°, 20°, 50° and temperatures of 6, 6, 3, 3 °C. This set of four APS runs produces acceptable errors for most observing conditions.

In current planning, every two to four weeks a few TMT mirror segments are swapped out for recoating, with each segment residing in the telescope two years or so. Thus a typical sensor in the telescope may have accumulated ten or twenty APS runs of data on which to base its calibration. Figure 7 illustrates this situation, with twenty APS runs at various zenith angles and temperatures marked by white circles. The temperatures were taken from Armazones (the baseline telescope site) site survey data.

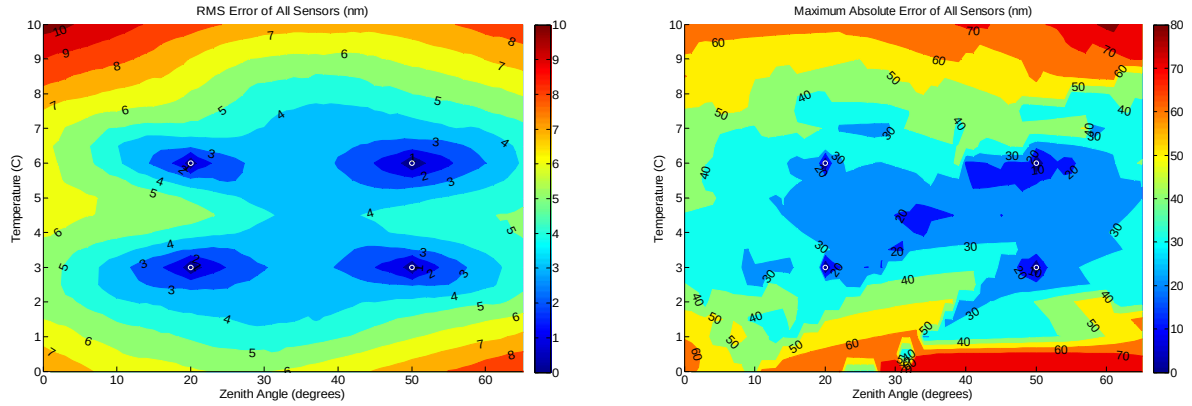

Figure 6. RMS (left) and Maximum (right) Absolute Calibration Error (nm), with 100 µrad rms sensor installation error and 5nm rms APS noise. APS zenith angles and temperatures are 20°, 50°, 20°, 50° and 6°, 6°, 3°, 3° C. The white circles mark the location of the APS runs.

In preparing Figure 7 it was assumed that all sensors have the same number of APS runs. In reality segments and their sensors will be rotated out for recoating, and a more realistic simulation is planned that will include varying numbers of APS runs for different sensors. The calibration procedures presented here do appear to have this flexibility, although this has not yet been demonstrated. A more realistic simulation will also better account for sensor drift, and include methods of dealing with drift such as deweighting older measurements.

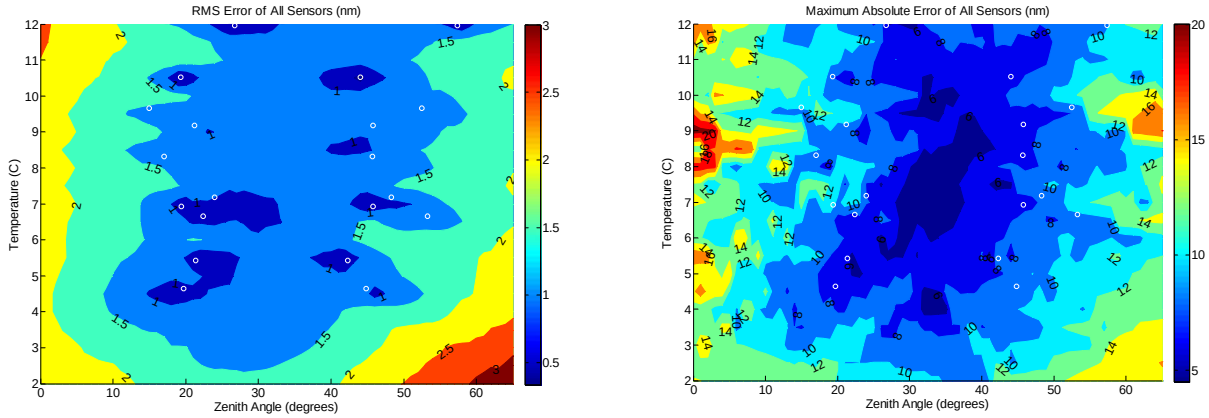

Figure 7. RMS (left) and Maximum (right) Absolute Calibration Error (nm), with 100 µrad rms sensor installation error and 5nm rms APS noise. There are twenty APS runs, at zenith angles and temperatures marked by white circles.

All the figures presented in this section use the sensor error in nm as a merit function. All the graphs shown in this section also show a maximum error over all sensors that is significantly larger than 5 nm. The mirror may or my not still meet image quality requirements with calibration-induced sensor errors of this magnitude. In planned future work, we will relate the calibration-induced sensor error to a wavefront error and to a point-spread function. Once a point spread function is computed, various imaging quality metrics can be applied such as encircled energy, full width half energy, etc. Such results will be more intuitive to the broader community, and will allow refining of the calibration procedure and sensor installation tolerances.

6.2 Performance as a Function of Sensor Installation Error

Figure 8 shows the average sensor calibration error (over zenith angles of 0° to 65° and temperatures from 0 to 10° C) as a function of sensor installation error. The dashed lines correspond to a sensor with a L_{eff} of 32 mm and the solid lines a L_{eff} of 15 mm. All of the plots in the previous section used a L_{eff} of 15 mm.

The black curves are the results when there is no calibration procedure. The data point at 10^{-4} radians is equivalent to the average of the data in the left hand plot of Fig. 2. The green curves are the results when there are two APS runs, one at 20° and another at 50° zenith angles, both at 3° C. These are the same conditions as in Fig. 3. The two APS runs help reduce the calibration error by about a factor of 10, but in order to reach less then 10 nm of calibration error the required sensor installation error is 10^{-5} radians.

The blue curves are the results when there are four APS runs at zenith angles 20°, 50°, 20° and 50° with corresponding temperatures of 6°, 6°, 3°, and 3° C. These are the same conditions as in Fig. 4. In this result ~6 nm of calibration error is reached at a sensor installation error of ~10^{-4} radians. It is also interesting to note that, while in general the sensor error increases linearly with L_{eff}, in this region the error is virtually identical for the two L_{eff} values analyzed.

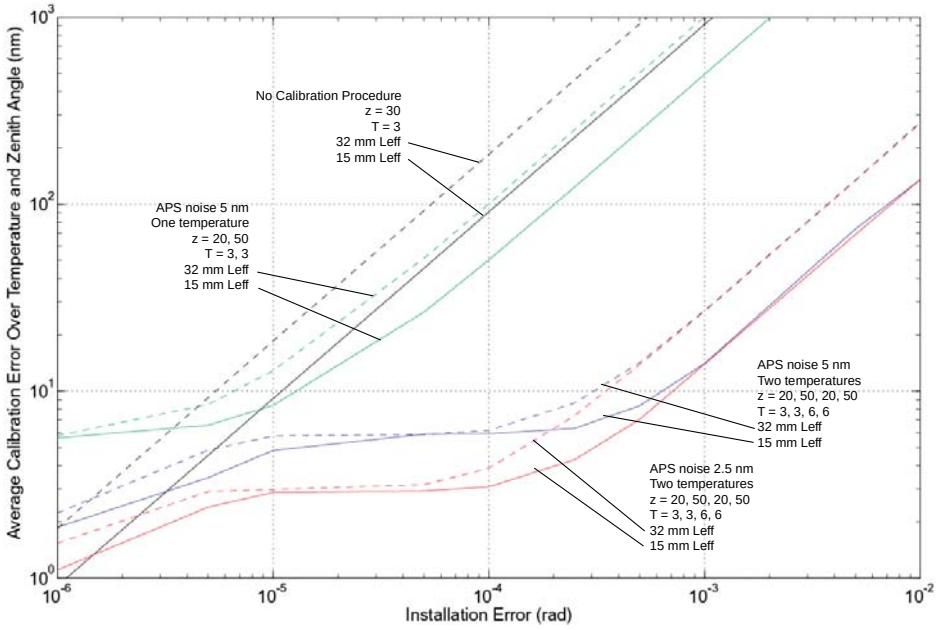

Figure 8. Average sensor calibration error (over zenith angles of 0° to 65° and temperatures from 0° to 10° C), as a function of sensor installation error. The dashed lines correspond to a sensor with a L_{eff} of 32 mm and the solid lines a L_{eff} of 15mm. The various cases are described in the text.

The red curves have the same parameters as the blue curves, except that the APS measurement noise has been reduced from 5 nm to 2.5 nm. The reduction by a factor of two of the APS measurement noise reduces the average sensor error by a factor of two.

7. CONCLUSIONS

The most important conclusion we can draw from this series of simulations is that an in-situ calibration procedure can be developed that will provide the required performance with practical limits on installation tolerances. Specifically, we conclude that a small number of APS runs with sufficient temperature diversity will give adequate capacitive edge sensor performance over all zenith angles and over a span of temperatures somewhat greater than that of the APS runs. For the calibration algorithm presented, and for the current TMT capacitive sensor concept, the required sensor installation errors are on the order of 10^{-4} radians.

This analysis also shows that measuring sensor offsets by varying only zenith angle does not give sufficient information to evaluate sensor cross terms, but that adding at least two APS runs at different temperatures will be adequate, with better results from repeated measurements.

While it is easy to attain data at different zenith angles, doing so at different temperatures is more problematic. There are several possible approaches to get getting significant temperature differences between APS runs. One method would be to take APS runs during evening twilight and morning twilight, when astronomical observations are not being conducted and there is commonly a significant temperature difference.

There are a number of areas in which the calibration process can be refined. The thermal model of the telescope is fairly simplistic, and a more realistic model needs to be utilized. Also, we need to investigate how averaging multiple APS observations can lower APS measurement noise, and how best to combine results from different APS runs. Finally, there may be methods for introducing in-plane segment motions besides using telescope zenith angle and temperature.

While the results presented here are specific to a particular capacitive edge sensor design, the calibration methodology has general applicability, and is being used to prepare a companion study for inductive edge sensors, and to point the way to improvements in the capacitive and inductive sensor designs. Preliminary results from the inductive study are favorable.

ACKNOWLEDGMENTS

This research was carried out in part at the Jet Propulsion Laboratory, California Institute of Technology, and was sponsored by the California Institute of Technology and the National Aeronautics and Space Administration. The authors gratefully acknowledge the support of the TMT partner institutions. They are the Association of Canadian Universities for Research in Astronomy (ACURA), the Association of Universities for Research in Astronomy (AURA), the California Institute of Technology and the University of California. This work was supported, as well, by the Canada Foundation for Innovation, the Gordon and Betty Moore Foundation, the National Optical Astronomy Observatory, which is operated by AURA under cooperative agreement with the National Science Foundation, the Ontario Ministry of Research and Innovation, and the National Research Council of Canada.

REFERENCES

The central archive of TMT documents (Docushare) is at tmt.org. TMT Reports and Technical Notes are available at tmt.ucolick.org.

[1] D. G. MacMartin, G. A. Chanan, “Control of the California Extremely Large Telescope primary mirror,” *Proc. SPIE* 4840, 69-80 (2003).
[2] Chanan, G., MacMartin, D.G., Nelson, J., and Mast, T., "Control and Alignment of Segmented-Mirror Telescopes: Matrices, Modes and Error Propagation", Applied Optics, Vol 43, No. 6, 1223-1232 (2004).
[3] MacMartin, D.G., and Chanan, G. "Measurement Accuracy in Control of Segmented-Mirror Telescopes", Applied Optics, Vol. 43, No. 3, 608-615 (2004).
[4] K. Szeto et al. “TMT telescope structure system: design and development progress,” *Proc. SPIE* 7012-88 (2008).
[5] Mast, T., Chanan, G., Nelson, J., Minor, R., Jared, R., “Edge sensor design for the TMT,” *Proc. SPIE* 6267, 62672S (2006).
[6] Terry Mast, “Report No. 77 - TMT Edge Sensor Concepts”, TMT.CTR.TEC.07.009.REL01 (2007).
[7] J. Nelson, “Edge Sensors: Abstract view,” TMT.PSC.PRE.07.004.DRF01 (2007).
[8] T. Mast, J. Nelson, “TMT Image Size and Wavefront Error Budgets”, TMT Report Number 10, Vol 2, TMT.OPT.TEC.07.022.REL01 (2007).
[9] G. Chanan, M. Troy, I. Crossfield, J. Nelson, and T. Mast, “The Alignment and Phasing System for the Thirty Meter Telescope,” *Proc. SPIE* 6267, pp. 62672V (2006).
[10] M. Troy et al., “A conceptual design for the Thirty Meter Telescope Alignment and Phasing System,” *Proc. SPIE* 7012-125 (2008).
[11] Shelton, C., Troy, M., Chanan, G., MacDonald, D., “M1CS Focus Mode Analysis”, TMT.CTR.TEC.07.019.REL01 (2007).

[12] Shelton, C., Roberts, L., Troy, M., Byoung-Joon Seo, “M1CS Capacitive Edge Sensor Calibration Analysis,” TMT.CTR.07.030.REL01 (2008).
[13] Jared, R., Minor, R., Doering, D., Van der Lippe, “Relative Humidity and the TMT Sensor,” TMT.CTR.PRE.07.010.REL01 (2007).
[14] Roberts, S., Sun, S., Kerley, D., "Optical performance analysis and optimization of large telescope structural designs", *Proc. SPIE* 5867, 200-211 (2005).
[15] Gary Chanan, “Segment In-Plane Position Sensing”, TMT.CTR.PRE.07.019.REL01 (2007).
[16] Vogiatzis, K., “Probabilistic Performance Analysis ‘Standard Year’”, TMT.SEN.PRE.07.030.DRF01 (2007).